Molecular Reconfiguration of Disordered Tellurium Oxide Transistors with Biomimetic Spectral Selectivity

Yuxuan Zhang, Jingwen Wang, Pengshan Xie, You Meng, He Shao, ChenXing Jin, Boxiang Gao, Yi Shen, Quan Quan, Yezhan Li, Weijun Wang, Dengji Li, Zenghui Wu, Bowen Li, SenPo Yip, Jia Sun,* and Johnny C. Ho*

Reconfigurable devices with field-effect transistor features and neuromorphic behaviors are promising for enhancing data processing capability and reducing power consumption in next-generation semiconductor platforms. However, commonly used 2D materials for reconfigurable devices require additional modulation terminals and suffer from complex and stringent operating rules to obtain specific functionalities. Here, a p-type disordered tellurium oxide is introduced that realizes dual-mode reconfigurability as a logic transistor and a neuromorphic device. Due to the disordered film surface, the enhanced adsorption of oxygen molecules and laser-induced desorption concurrently regulate the carrier concentration in the channel. The device exhibits high-performance p-type characteristics with a field-effect hole mobility of 10.02 cm^2 V^{-1} s^{-1} and an I_{on}/I_{off} ratio exceeding 10^6 in the transistor mode. As a neuromorphic device, the vision system exhibits biomimetic bee vision, explicitly responding to the blue-to-ultraviolet light. Finally, in-sensor denoising and invisible image recognition in static and dynamic scenarios are achieved.

1. Introduction

As silicon-based technology approaches its physical limits, further miniaturization of electronic circuitry is hindered.[1] To achieve higher computational complexity with the same level of integration, it is essential to design devices based on structural innovations or new physical mechanisms.[2–9] Reconfigurable devices, which possess multiple functions and can switch their specific characteristics for different tasks, have proven effective. Layered 2D semiconductors and 1D nanowires have been explored for reconfigurable devices.[10–15] Controllable doping of channel materials is crucial for achieving reconfigurable functionalities. Due to their unique electronic properties and excellent electrostatic control, low-dimensional materials can accommodate various modifying strategies. These include defect engineering,[16,17] electrostatic gating,[18] ferroelectric polarization,[19] and ion-mediated dynamics.[20,21] However, implementing these strategies often involves complex fabrication processes that increase the manufacturing cost. In addition, the switch between logic transistors and artificial synapses typically requires an extra de-trapping process and precisely tuned photoelectric or multi-gate coupled stimulation.[22,23] The rigorous operating rules for achieving specific working modes further challenge integration versatility and the extension of device functions.

Unlike highly crystalline low-dimensional semiconductors, amorphous oxide semiconductors (AOSs) offer unique advantages in terms of manufacturing cost, large-area uniformity, and electronic structure.[24] The direction-independent orbital overlap in the amorphous network forms a carrier percolation pathway, resulting in higher electron mobility (>10 cm^2 V^{-1} s^{-1}) than in traditional silicon-based materials.[25] These AOSs are currently applied in large-area circuits and displays, and heterostructures or interface defects designed to modulate channel conductance are also employed to construct emerging neuromorphic networks.[26–29] Various materials, such as metal oxides, have been reported to exhibit neuromorphic behaviors in response to light ranging from the visible to ultraviolet spectra. However, most AOSs are limited to simple device structures, achieving only

Y. Zhang, P. Xie, Y. Meng, H. Shao, B. Gao, Y. Shen, Q. Quan, Y. Li,
W. Wang, D. Li, Z. Wu, B. Li, J. C. Ho
Department of Materials Science and Engineering
City University of Hong Kong
Hong Kong SAR 999077, P. R. China
E-mail: johnnyho@cityu.edu.hk

J. Wang, C. Jin, J. Sun
Hunan Key Laboratory for Supermicrostructure and Ultrafast Process
School of Physics and Electronics
Central South University Changsha
Hunan 410083, P. R. China
E-mail: jiasun@csu.edu.cn

Y. Meng, J. C. Ho
State Key Laboratory of Terahertz and Millimeter Waves
City University of Hong Kong
Hong Kong SAR 999077, P. R. China

S. Yip, J. C. Ho
Institute for Materials Chemistry and Engineering
Kyushu University
Fukuoka 816 8580, Japan

J. Sun
State Key Laboratory of Transducer Technology
Shanghai Institute of Microsystem and Information Technology
Shanghai 200050, P. R. China

**ADVANCED
SCIENCE NEWS**

www.advancedsciencenews.com

**ADVANCED
MATERIALS**

www.advmat.de

single functions, and exhibit n-type dominant electrical characteristics, with p-type counterparts still being elusive.[30] Recent reports on crystalline and amorphous tellurium oxide thin films as p-type semiconductors have demonstrated excellent hole transport properties.[31,32] However, these studies primarily focus on the material's intrinsic properties, overlooking potential surface interactions with the environment, which limits the multifunctionality of p-type oxide semiconductors. Surface interactions with the environment can induce new electrical phenomena that enable diverse functionalities,[33,34] which is promising but has yet to be explored in reconfigurable devices.

In this work, we report a new type of AOS based on the disordered tellurium oxide (DTO), where the oxygen implantation during room-temperature deposition retards the crystallization process. The DTO film shows a molecularly switchable behavior with a dual-mode feature that can switch between a logic transistor and a neuromorphic device. Density functional calculations (DFT) suggest that the reconfigurable behavior originates from the adsorption/desorption of oxygen on the disordered TeO_x surface. The intrinsic p-type characteristic in vacuum presents a respectable field-effect hole mobility of 10.02 cm^2 V^{-1} s^{-1} and a high I_{on}/I_{off} ratio exceeding $\approx 10^6$. We fabricate basic logic gates using the DTO film (e.g., inverter, NAND, and NOR gates) to demonstrate its adaptability with large-area circuits composed of complementary metal-oxide-semiconductors (CMOS). As a neuromorphic device, the DTO-based vision system shows specific responses to short-wavelength light, mimicking the vision of bees. Leveraging this characteristic, we develop an artificial visual network that demonstrates in-sensor denoising capabilities and recognition of images unobservable to human eyes.

2. Results and Discussions

2.1. Operating Mechanism of the DTO Device

The main working principle that realizes the reconfiguration between the logic and neuromorphic device of our DTO device lies in the enhanced gas adsorption due to the defective surface structure and photoinduced desorption (**Figure** 1a). It is well known that electrons at the valence band maximum (VBM) of the underlying semiconductor will migrate to the lowest unoccupied molecular orbital (LUMO) of the adsorbed gas in air (e.g., O_2 and H_2O) due to its higher electron affinity.[35] The discernable difference in the counterclockwise hysteresis of transfer curves measured in air and vacuum further confirms the impact of gas adsorption (Figure 1b). The DFT calculation compares the interactions of gases with crystallized Te and amorphous TeO_x surfaces. Detailed structural analyses are provided in Note S1 (Supporting Information). Charge analyses of the gas adsorption on tellurium and amorphous TeO_x are shown in Figure 1c,d and Figure S2a,b (Supporting Information) (left panel). The spatial charge distribution of oxygen adsorption shows that the charge is mainly confined near the oxygen on the Te surface. However, the orbital hybridization, with a smaller adsorption distance, is more prominent on the TeO_x surface. Meanwhile, the differential charge density visualizing the charge transfer in Figure 1c,d and Figure S2a,b (Supporting Information) (right panel) indicates an enhancement in charge transfer. The lower adsorption energy and enormous charge transfer quantified in

Figure 1e also indicate the favorable adsorption of O_2 on the disordered TeO_x. In the case of H_2O adsorption, the calculation yields similar results (Figure S2c, Supporting Information), except that the charge transfer on the TeO_x surface is not significantly different from that on the Te surface, which indicates that the O_2 adsorption primarily contributes to surface interactions on TeO_x. The reversibility of the molecular reconfiguration strategy is validated by the successive switching between the transistor mode and the neuromorphic mode several times. In Figure S3 (Supporting Information), the change in hysteresis width confirms the reversible surface interactions on the DTO surface and the reproducible dual-mode functionality of the device.

Here, a mechanism is proposed where the realization of the neuromorphic vision device arises from the competition between the photogenerated carriers and the surface interaction of O_2 molecules. As shown in Figure 1f, in the dark environment, electron transfer to O_2 results in p-type doping of the channel. Under pulsed light illumination, incredibly short-wavelength light, the photon energy accelerates the O_2 desorption, which releases trapped electrons that partially combine with photoinduced holes due to the photoconductive effect (Figure 1g). Such a process effectively modulates the carrier concentration in the channel, leading to a monotonic variation of the conductance state under continual light stimuli. After turning off the light, holes released from the re-adsorbed O_2 counteract the fast recombination of electron–hole pairs (Figure 1h), prolonging the time for the system to return to its original electrical state, analogous to the long-term potentiation (LTP) in a neuron. These mechanisms endow the DTO film with tunable doping levels and, thus, behavior-emulating biological visual neurons. In the absence of O_2 regulation of the carrier concentration, the carrier concentration can only be modulated by the gate terminal, and the electrical properties are dominated by the intrinsic properties of DTO. Hence, the surface process is pivotal for the dual-mode switch between transistors and neuromorphic devices.

2.2. Characterization of the DTO Film

Unlike highly-ordered hexagonal tellurium, the amorphous phase of DTO provides abundant defect sites for the gas interaction. Since deposited tellurium can crystalize uncontrollably at ambient temperature,[36] and the subsequent oxidation cannot amorphize tellurium,[37] we directly implant oxygen into the film matrix during deposition. The oxygen implantation suppresses the crystallization process by increasing the degree of inhomogeneity due to the large discrepancy in atomic radii of tellurium and oxygen (Figure S4, Supporting Information). Hence, this oxygen-induced amorphization effect results in the loss of long-range order and impedes the spontaneous arrangement of helical tellurium chains. Grazing-incidence X-ray diffraction (GI-XRD) patterns (Figure S5a, Supporting Information) show that the as-deposited DTO is amorphous, while a weak (101) peak emerges after a mild annealing condition at 150 °C. This new peak indicates a mixed phase that consists of hexagonal phase Te and substoichiometric TeO_x. Without oxygen acting as a crystallization alleviator, the polycrystalline tellurium is observed after deposition (Figure S6, Supporting Information).
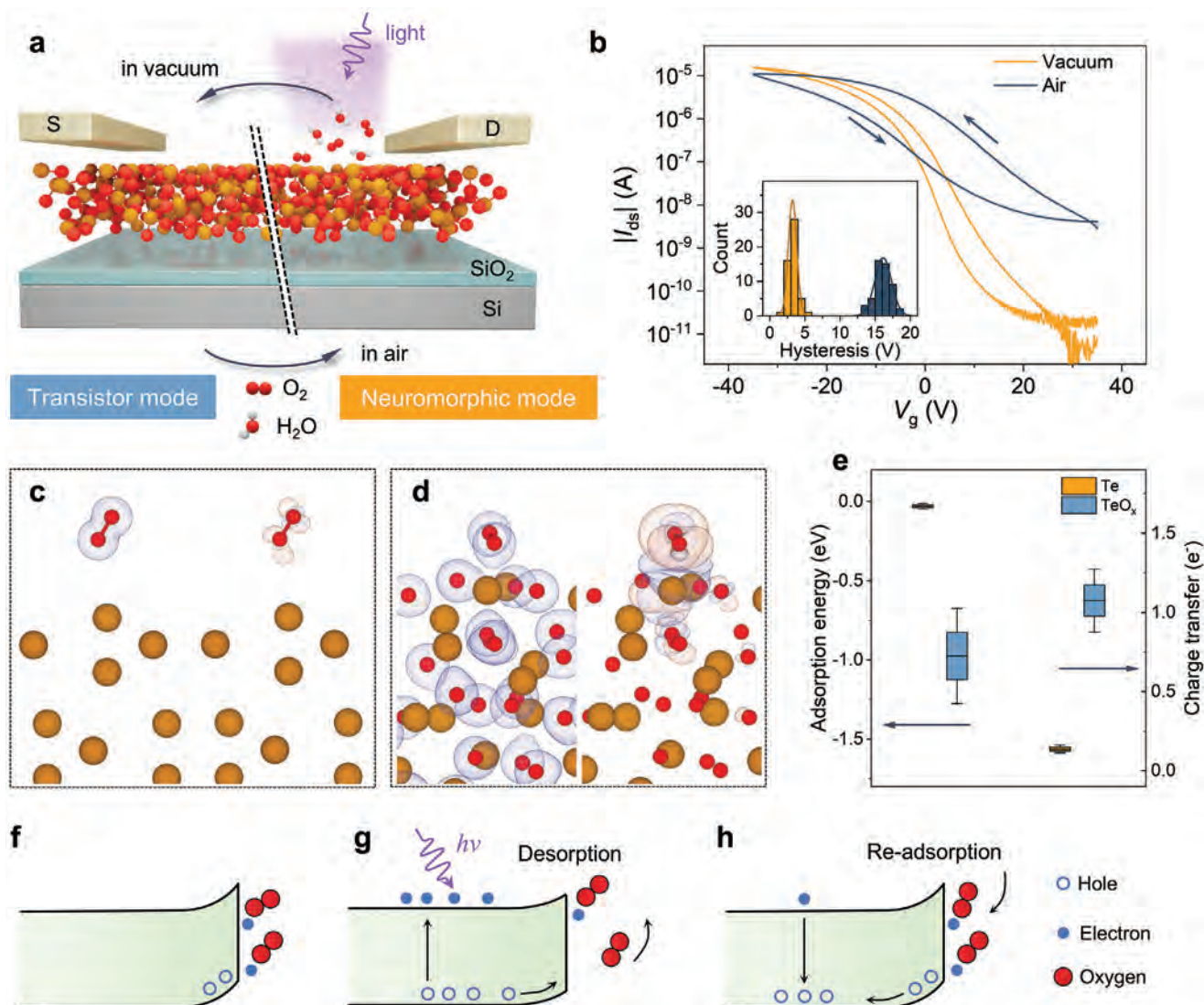
Figure 1. Schematic and working principle of the DTO device. a) Schematic illustration of a molecularly reconfigurable DTO device. b) Transfer characteristics of the DTO device in vacuum and air at $V_{ds} = -1$ V. Inset is the statistic distributions of hysteresis in vacuum and air. c,d) The charge density (left panel) from the conduction band and valence band and the differential charge density (right panel) of the oxygen adsorption on c) Te and d) TeO$_x$. The brownish-red and blue regions in differential charge density indicate electron accumulation and depletion, respectively. Isosurface levels are 0.1 and 0.002 e Bohr^{-3} for charge density and differential charge density, respectively. e) The adsorption energy and charge transfer from oxygen to the surface, as determined by Bader charge analysis. f–h) Schematic of the oxygen-mediated carrier concentration modulation that can be used to emulate behaviors of optical neurons.

The high-resolution transmission electron microscopy (HRTEM) illustrates a large area of amorphous oxidized tellurium (Figure S5b, Supporting Information). Meanwhile, the diffraction pattern and enlarged TEM images further confirm the presence of Te polycrystals embedded in the matrix (Figure S7a–d, Supporting Information). The corresponding cross-sectional TEM image exhibits the uniform distribution of O and complete oxidation of the film (Figure S7e, Supporting Information). X-ray photoelectron spectroscopy (XPS) analysis reveals the coexistence of Te^{4+} and Te^0 peaks (Figure S8a, Supporting Information), indicating that a large portion of Te is oxidized as O—Te—O. Further oxidation can be achieved by the post-annealing as the ratio of Te^{4+}/(Te^0+Te^{4+}) increases

from 66.37% to 81.73% after 150 °C annealing. In Figure S8b (Supporting Information), a small peak associated with adsorbed oxygen species can be observed, and this peak disappears after an Ar$^+$-etching process, validating the gas adsorption of the DTO film. The surface profile is characterized using atomic force microscopy (AFM). Before and after mild annealing, all deposited films show good homogeneity without discernible voids (Figure S9a–d, Supporting Information). The standard deviation roughness (R_a) slightly decreases as the annealing temperature rises to 150 °C and increases to 0.31 nm after annealing at 200 °C (Figure S9e, Supporting Information). The heat treatment mitigates the short-range disorder and flattens the surface, improving the film quality (Figure S9f, Supporting Information). However,

**ADVANCED
SCIENCE NEWS**

www.advancedsciencenews.com

**ADVANCED
MATERIALS**

www.advmat.de

excessively high temperatures induce the evaporation of Te due to its high saturated vapor pressure,[38] which results in minor surface roughening. The extracted bandgap is approximately 1.05 eV, slightly larger than the theoretical value of 0.73 eV (Figure S10, Supporting Information). Notably, in Figure S10a (Supporting Information), the 150 °C-annealed DTO film shows strong and unique absorption at a wavelength below 330 nm, similar to previously reported tellurium oxide films.[39,40] Additionally, the higher energy of UV light generates more photogenerated holes in the channel, leading to a significant increase in photocurrent. Thus, the DTO film has an enhanced photoresponse in the blue-to-ultraviolet range and the potential for blue-to-ultraviolet image recognition. Different from conventional crystalline p-type semiconductors where orbitals are highly directional and localized near the VBM,[30,41–43] the electronic density of states of the DTO demonstrates delocalized p orbitals near the VBM (Figure S11, Supporting Information). The spatially spread and hybridized Te 5p and O 2p orbitals can serve as shallow acceptors and facilitate hole transport.[31] Combined with the high hole mobility of embedded Te (707 cm^2 V^{-1} s^{-1}),[44] the high-performance p-type transistor can be realized. To investigate the relationship between the amorphous degree of DTO and its electrical properties, we constructed various amorphous TeO models using a melt-quench-relaxation approach based on ab initio molecular dynamics. As the degree of amorphization increases, the p orbitals near the VBM become more dispersed. In contrast, for sub-stoichiometric tellurium oxide without disordering treatment, the VBM is predominantly dominated by localized O-2p states (Figure S12a, Supporting Information). These results are further corroborated by the charge density distribution near the Fermi level (Figure S12b–d, Supporting Information). Thus, achieving effective amorphization in DTO can significantly enhance its transistor performance.

2.3. Transport Performance of DTO in Transistor Mode

The switch to transistor mode is achieved by excluding oxygen. The DTO film exhibits its intrinsic transport properties in a typical thin film transistor device with a simple structure of bottom gates and top contacts in this configuration. Transfer curves of DTO films with various annealing temperatures and thicknesses are shown in **Figure 2a** and Figure S13 (Supporting Information). The as-deposited sample exhibits poor transfer performance, likely due to the loose structure that intensifies carrier scattering. This leads to reduced conductivity and mobility. Notably, annealing at low temperatures significantly improves the p-type transfer characteristics, accompanied by a positive shift in the threshold voltage. In Figure 2b, the annealing at 150 °C yields the highest I_{on}/I_{off} ratio and hole field-effect mobility of ≈10^6 and 10.02 cm^2 V^{-1} s^{-1}, respectively. The decent I_{on}/I_{off} ratio can be ascribed to the enlarged bandgap resulting from oxygen incorporation, rendering a lower off current. In stark contrast, devices with directly deposited elemental Te show a small I_{on}/I_{off} ratio (≈10^3; Figure S14, Supporting Information) due to the narrow bulk bandgap (0.35 eV).[45] Due to the scalable deposition technique, transfer curves from 50 individual devices highlight the negligible device-to-device variability (Figure 2c). Besides, the linear output characteristics at low source–drain volt-

ages indicate an Ohmic contact at the channel-electrode interface (Figure 2d). The transmission-line method is used to evaluate the contact resistance (R_c), yielding a value of 571 Ω cm (Figure S15, Supporting Information). This relatively low R_c ensures the transistor performance and the soundness of the extraction of field-effect mobility. Hence, the overall transistor performance surpasses most p-channel transistors (e.g., metal oxides, metal halides, and perovskites; Table S1, Supporting Information). Temperature-dependent transfer curves and mobilities are measured to investigate the underlying carrier scattering mechanisms (Figure 2e,f). At lower temperatures, the subthreshold swing becomes smaller. In comparison, at higher temperatures ($T > 200$ K), the mobility exhibits a typical phonon-scattering-limited transport, as evidenced by the power law dependence of the mobility curve ($\mu \propto T^{-\gamma}$, where γ is fitted to be 0.30). The DTO-based device operating in transistor mode is remarkably stable under a 1500 s on/off cycling test. After 300 consecutive sweeps, the transfer characteristics, I_{on}/I_{off} ratio, and on-current are well sustained (Figure 2g,h). Moreover, one batch deposition of the DTO film costs approximately 1.4 USD for the source powder, and the fabrication takes only a few minutes. These results indicate that DTO devices exhibit excellent stability, scalability, and a high cost-benefit ratio. Further improvements in stability and applicability for large-scale integration can be achieved through synergistic optimization of the device structure, dielectric materials, evaporation process, and fabrication techniques.

Benefiting from uniform and large-area production, the reconfigurable DTO device in transistor mode can be integrated with n-type metal-oxide as building blocks for CMOS logic circuits (**Figure 3a**). Figure 3b illustrates the optical image and diagram of an inverter composed of the p-type DTO film and the well-developed n-type In$_2$O$_3$ transistor. The In$_2$O$_3$ is prepared by magnetron sputtering, with detailed processes provided in the Experimental section, and a typical transfer curve is provided in Figure S16 (Supporting Information). The voltage swing in Figure 3c demonstrates a highly symmetrical shape and a distinct logic transition, indicative of the inverter function. The total noise margin (NM = (NM$_H$ + NM$_L$)/V_{dd}), extracted from the mirror reflection area, is 77% at $V_{dd} = 10$ V. The inverter also delivers a peak gain of 8.5, essential for signal propagation in cascade circuits.[46,47] Other complementary logic gates, such as NAND and NOR, are also fabricated (Figure 3d,g). The output characteristics plotted in Figure 3e,h show the desired Boolean functionalities. Moreover, 2D manifestations of logic states as functions of V_{i1} and V_{i2} are presented in Figure 3f,i, agreeing well with the corresponding truth tables (Figure S17, Supporting Information). The successful realization of these logic gates demonstrates the full functionality of the reconfigurable DTO film in transistor-mode operation.

2.4. Emulating Bee Vision for Image Recognition with DTO in Neuromorphic Mode

The neuromorphic functionality of the DTO film can be achieved in an ambient atmosphere. Due to the higher sensitivity of DTO films to UV wavelengths, neuromorphic DTO devices have been further investigated for image recognition and processing. **Figure 4a,b** show typical synaptic plasticity in postsynaptic
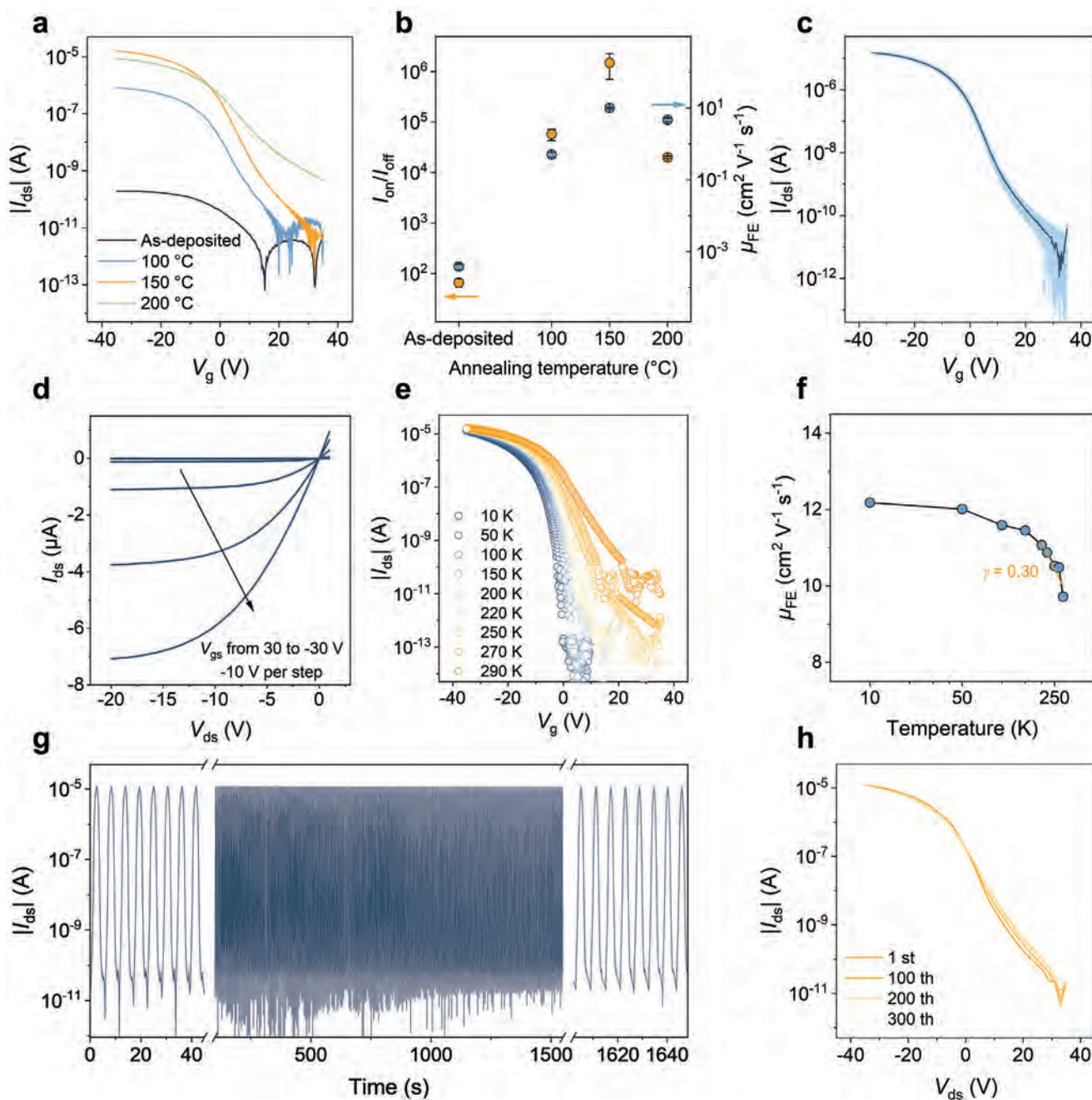
Figure 2. Electrical measurements in the transistor mode. a) Transfer curves of DTO transistors as a function of annealing temperature. b) Summary of the I_{on}/I_{off} ratio and field-effect hole mobility corresponding to (a). c) Transfer curves of 50 individual transistors fabricated using the optimized condition. d) Output curves of the optimized transistor. e) Temperature-dependent transfer curves and f) corresponding mobilities of the DTO transistor. g) Continuous on/off switching measurement. h) Representative transfer curves after different cycling tests.

currents (PSC) under varying light pulse intensities and durations. Upon UV stimulation, the PSC gradually decreases after reaching a peak and stabilizes at different postsynaptic signal levels depending on the stimulation conditions. This indicates the LTP of the DTO film and its potential applications in in-sensor computing and processing. The PSC can also be triggered by visible light spikes (Figure S18, Supporting Information). However, under low light conditions, the weight update

of PSC induced by visible light is much weaker than that induced by UV light (Figure 4c). This wavelength selectivity is analogous to the trichromatic vision of bees. A 5 × 5 sensing array composed of DTO devices is able to recognize the input pattern (Figure 4d–f). The illuminated pixels gain higher PSC than masked pixels, and the current gradually decreases over time (Figure 4g–i), demonstrating a nonvolatile memory feature.
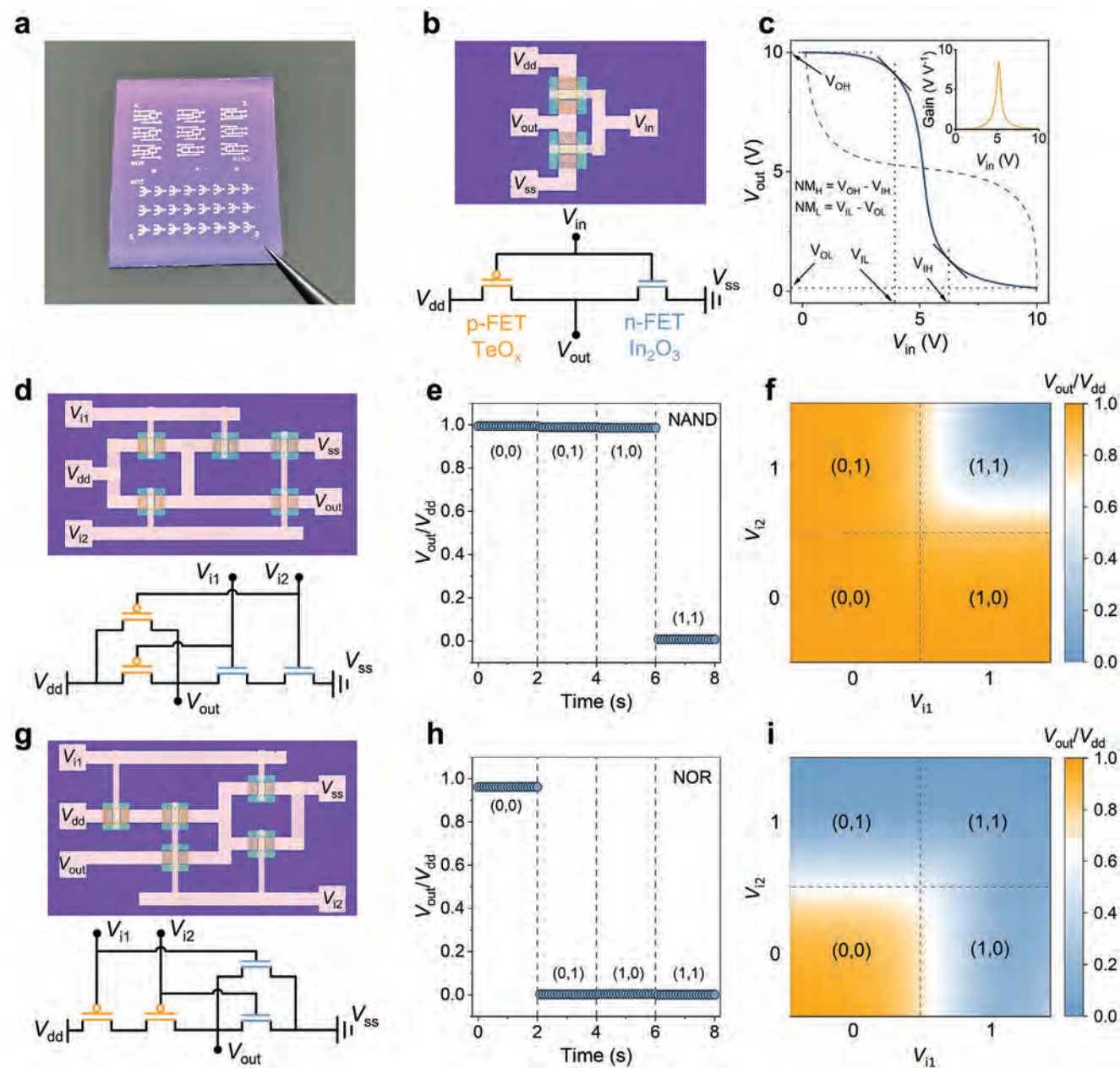
**ADVANCED
SCIENCE NEWS**

www.advancedsciencenews.com

**ADVANCED
MATERIALS**

www.advmat.de

Figure 3. Demonstration of CMOS logic circuits. a) Photograph of CMOS logic gates on a rigid Si/SiO$_2$ substrate. b) Optical micrograph and schematic diagram of the inverter. c) Output curves and voltage gain as a function of input voltage (V_{in}) for the inverter. Optical micrographs and schematic diagrams of d) the logic NAND and g) NOR gates. Output voltages of e) the logic NAND and h) NOR gates at four typical input states. Operations of f) NAND and i) NOR gates with different V_{i1} and V_{i2} values.

Flowers depend on insects, such as bees, for pollination, while bees feed on nectar and pollen. Thus, flowers have evolved ultraviolet (UV) color patterns on their petals to help bees target the areas of nectar.[48] The ultraviolet signals emitted by an object can stimulate the photoreceptors in the compound eyes of bees while eliciting weak responses to other wavelengths. This allows humans to perceive imperceptible ultraviolet information (**Figure 5a**). Inspired by the wavelength-selective neuroplasticity of bee vision, we utilize a DTO-based neuromorphic device to en-

able the extraction of short-wavelength light details. In Figure 5b, the device array acts as a weight matrix (convolution kernel) that performs convolution operations. Detailed procedures are provided in Note S2 (Supporting Information). An artificial neural network (ANN) with 748 input neurons, 100 hidden neurons, and 10 output neurons is subsequently used for image recognition. Notably, the PSC quickly saturates under multiple laser pulse stimulations in a vacuum, significantly weakening the neuromorphic characteristics (Figure S19, Supporting Information). This
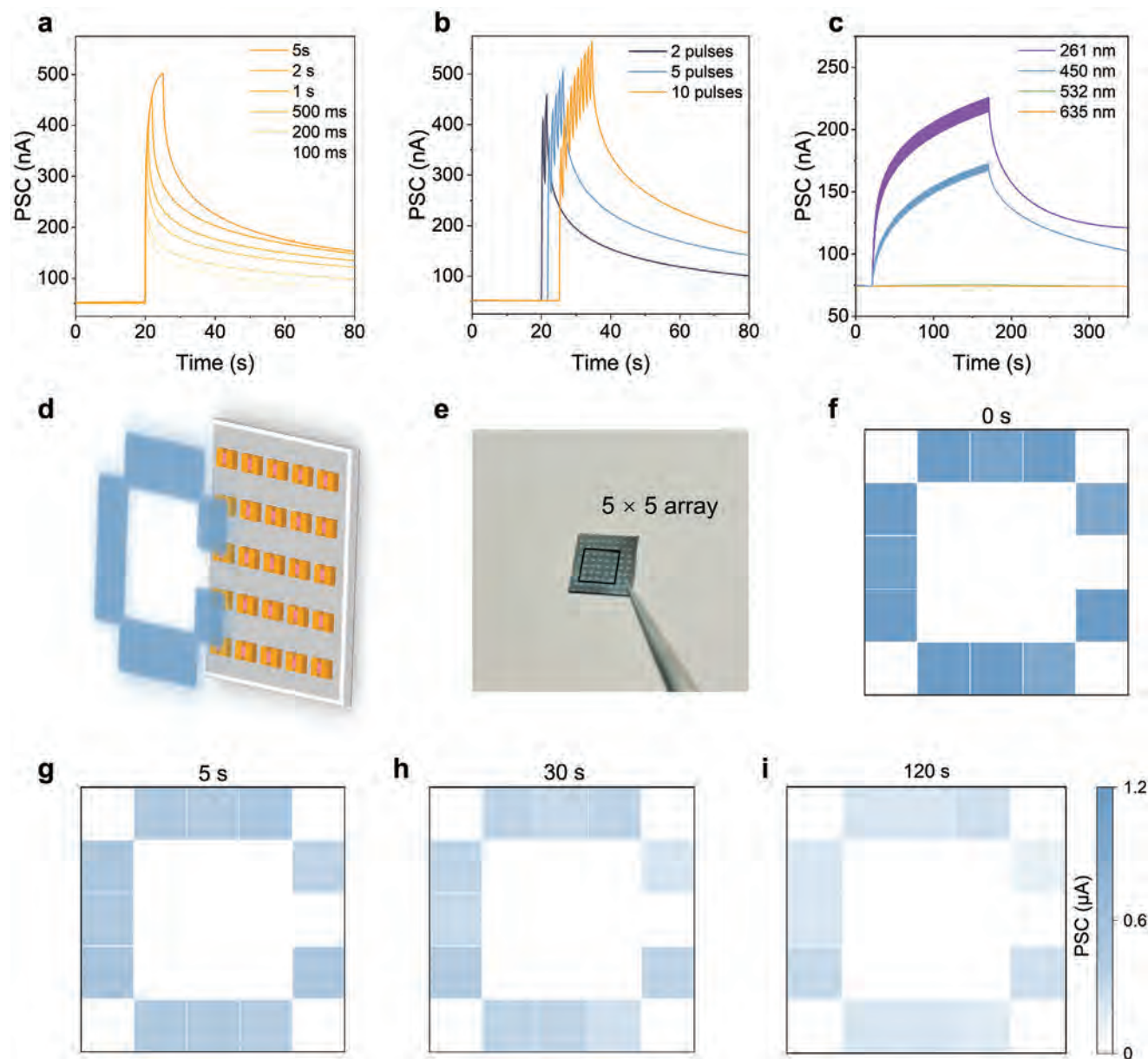
Figure 4. Synaptic plasticity and image recognition of DTO films working as neuromorphic devices. Postsynaptic current of synaptic DTO device triggered by a) different pulse widths and b) pulse numbers for 261 nm laser. The light intensity is 0.24 mW cm^{-2}. c) Post synaptic current triggered by various wavelength illuminations at low-light conditions (6 µW cm^{-2}). d) Schematic of a 5 × 5 pixel array in the UV image processing. e) Photograph of the DTO-based sensor array. f–i) Image recognition and memory of the device array with an input image of letter C.

indicates the role of gas adsorption/desorption in modulating channel carrier concentration and enabling device neuromorphic functionality.

During image recognition, the ANN is trained using handwritten digit images from the Mixed National Institute of Standards and Technology (MNIST) database. Three types of test datasets (including original MNIST datasets, datasets with added red and green (RG) Gaussian noise, and preprocessed datasets) are then input into the ANN for recognition. The minor difference in confusion matrices between the original dataset and the dataset preprocessed with the UV band (261 nm) highlights the effective-

ness of the device array in in-sensor denoising and extracting ultraviolet light information (Figure 5c,d). The results for the dataset preprocessed at the 450 nm band are shown in Figure S20 (Supporting Information). The recognition accuracy with training epochs is displayed in Figure 5e, where the dataset with RG Gaussian noise had a recognition accuracy of only 11%. In comparison, the preprocessed dataset recognition accuracy improved to 97%, close to the 93% accuracy of the original MNIST dataset.

Next, we demonstrate the motion detection of a small ball with UV patterns in dynamic scenes (Figure 5f and Movie S1, Supporting Information). In UV vision, the device array enhances the
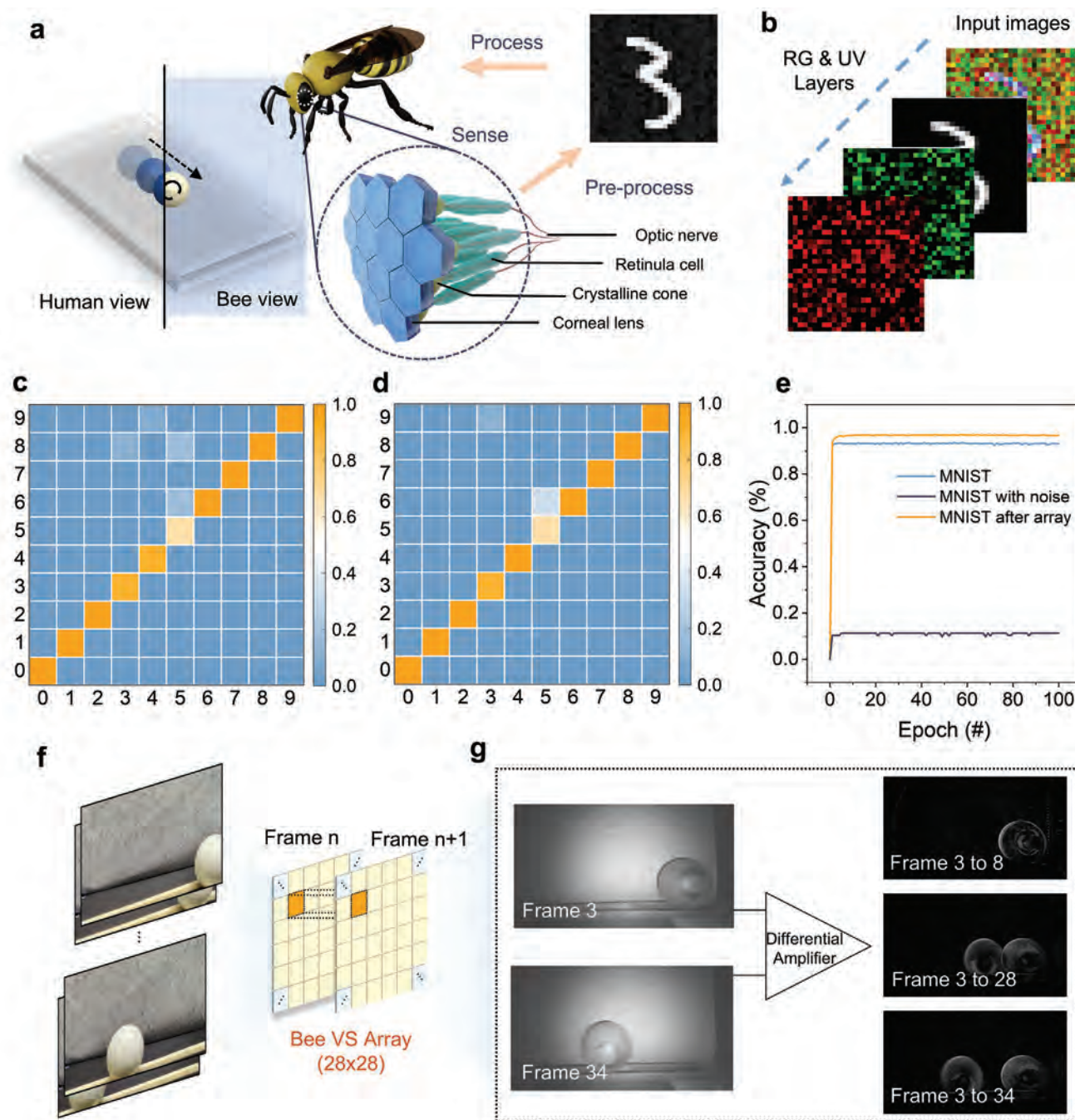
Figure 5. Image recognition in static and dynamic scenes inspired by bees. a) Illustration of the detection of ultraviolet patterns and corresponding biological system of bee vision. b) Construction of digital images with noises for image processing in ANN. Confusion matrices of classification for c) original images and noised images with preprocessed images with d) 261 nm light information. e) Variations in the recognition accuracy as the function of training epoch in different conditions. Illustration of f) invisible pattern motion and results from g) different time intervals.

pattern previously invisible to the human eye while surrounding signals are almost suppressed (Movie S2, Supporting Information). The processed video is divided into 60 frames at 33 ms intervals, and frame-difference calculations are introduced.[49] By computing the difference in response between the UV-sensed image and the stored image at times t and $t + \Delta t$, the static pixels corresponding to objects that did not move during Δt

are suppressed to nearly zero. For moments with moving objects, the output image contains information about the moving objects at both time points. Motion detection results vary with different Δt values, as shown in Figure 5g for Δt intervals of 5, 23, and 31 frames. When Δt is one frame, the motion detection result is presented in Movie S3 (Supporting Information). The results validate that the DTO-based biomimetic

**ADVANCED
SCIENCE NEWS**

www.advancedsciencenews.com

**ADVANCED
MATERIALS**

www.advmat.de

sensor array can capture UV information in static and dynamic circumstances.

3. Conclusions

We have reported a molecularly reconfigurable device based on amorphous tellurium oxide. The switch between logic transistors and neuromorphic vision devices is accomplished by the competition between the photogenerated carriers and the oxygen adsorption/desorption on the disordered surface. The intrinsic p-type transport, without the effect of oxygen molecules, delivers outstanding electrical performance with good scalability and stability. Several cascaded logic gates have also been demonstrated, indicating the potential for simplifying circuitry with advanced functionalities. Light stimulation and oxygen adsorption concurrently modulate the carrier concentration, and the DTO film shows specific responses to short-wavelength UV light. Inspired by the biological behavior of bees collecting nectar using UV signals, we employ a DTO-based sensory array and achieve biorealistic bee vision that successfully extracts UV information through a convolutional neural network.

To integrate DTO devices showing different behaviors in a single chip for complex signal processing, the widely used vacuum packaging technology in microelectromechanical systems can be applied. This method is highly compatible with our reconfigurable devices. It can create suitable microenvironments for different devices on the same chip, achieving transistor and neuromorphic functionalities in the same environment (Note S3, Supporting Information). Notably, despite many reconfigurable devices that integrate various functions, there is currently a lack of strategies to fabricate reconfigurable devices using simple structures and scalable methods. Furthermore, few studies have reported the ability to achieve both logic circuits and neuromorphic devices. Our DTO fabrication method offers advantages over laborious mechanical exfoliation and achieves more comprehensive functionality (Table S2, Supporting Information). Therefore, our molecularly reconfigurable logic devices and neuromorphic vision system not only enhance the computational efficiency to meet more complex computational demands but also possess a fabrication method compatible with modern semiconductor processes. This compatibility can effectively reduce design and manufacturing costs, providing significant potential for scalability and commercialization.

4. Experimental Section

Film Fabrication and Characterization: The deposition of DTO films was carried out at ambient temperatures in a high vacuum chamber pressure of 2×10^{-6} Torr. In a typical deposition process, 350 mg TeO_2 powder (J&K Scientific, 99.99%) was directly loaded in a tungsten boat and used as an evaporation source. The evaporation rate was controlled to be around 1.5 Å s^{-1}. The film was monitored by the quartz crystal microbalance, and the shutter was used to control the desired film thickness. The as-deposited samples were annealed on the hot plate for 1 hour in air before device fabrication. The crystallinity and phase composition of the ultra-thin films were revealed by the GI-XRD (Rigaku Smartlab) with the grazing-incident angle fixed to be 1°. The hybrid phase composition was characterized by HRTEM images using Talos F200S. The element distribution was analyzed using the Super-X detection system attached to the transmission electron microscopy. To obtain the chemical analysis of the surface, XPS was conducted by a Thermo ESCLAB 250Xi system with Ar$^+$ ion etching. The film topography and the roughness were evaluated by AFM (MultiMode 8, Bruker). The Raman spectra were collected by the confocal microscope spectrometer (Alpha 300R, WITec). The adsorption spectra were measured by the UV-Vis-NIR spectrophotometer (UH4150).

DFT Calculation: The Ab initio calculations were performed within the DFT framework with the Vienna Ab-initio Simulation Package (VASP).[50] The electron–electron exchange-correlation energy was approximated by the generalized gradient approximation (GGA) with the Perdew-Burke-Ernzerhof (PBE) functional.[51] Projected augmented wave potentials were used to describe core-level electron wave functions. The amorphous TeO_x was modeled by a melt-quench-relaxation method in a supercell that contains 54 Te atoms and 90 oxygen atoms based on the atomic ratio from XPS analysis. In detail, the initial atomic positions were randomized by melting at 3000 K for 10 ps and then quenched from 1500 to 300 K with a cooling rate of -100 K ps^{-1}. The model was further relaxed until the atomic forces were less than 10^{-2} eV Å^{-1}. The cutoff energy of 450 eV and the convergence criterion for the self-consistent calculation of 10^{-4} eV were used. For the Brillouin zone sampling, the Γ point was used for ab initio dynamic calculation, and a $3 \times 3 \times 3$ grid mesh was used for electronic structure calculation. The differential charge density was derived by subtracting TeO_x and gas molecule charge density from the post-adsorption charge density.

Device Fabrication: The DTO film was deposited on a heavily doped Si wafer with a 50 nm thermally grown SiO_2 as the dielectric layer. The 50 nm thick Ni was deposited as source and drain electrodes via electron beam evaporation, and both the channel length and width were 100 μm. Both channel materials and electrodes were patterned by shadow masks to reduce potential gate leakage current. For the integration of logic gates, each layer's pattern was aligned with the substrate and the previous layer using a designed shadow mask. The laser-cut mask was manually aligned via a mechanical aligner equipped with a microscope. The aligned shadow mask was then fixed onto the substrate for the subsequent deposition steps. Specifically, we employed atomic layer deposition (ALD) to grow a 10 nm HfO_2 layer as the dielectric layer for the bottom gate. The n-channel In_2O_3 was fabricated by magnetic sputtering. Before sputtering, the chamber was pumped to 5×10^{-6} Torr. Then, pure oxygen and argon were blended at flow rates of 4 and 40 sccm, respectively, and the working pressure was raised to 7×10^{-3} Torr. The sputtering power was set to 50 W, and the sputtering time was 2 min.

Reconfiguration and Electrical Measurement: The DTO in transistor mode was achieved in a chamber with a base pressure of 1×10^{-6} Torr, and the electrical characteristic measurements were performed using a semiconductor parameter analyzer (Agilent B1500A). Field-effect mobility (μ_{FE}) was extracted in the linear regime using $\mu_{FE} = Lg_m/(WCV_{ds})$, where L, W, and C were the channel length, width, and gate capacitance of the SiO_2 dielectric layer, respectively. The g_m was the transconductance ($\partial I_{ds}/\partial V_g$). The temperature-dependent electrical features were measured in a cryogenic probe station (Lake Shore CRX VF). The optoelectronic properties in the neuromorphic mode were tested in ambient air. The lasers (261, 450, 532, and 635 nm) were guided by an optical fiber and were calibrated by a power meter (PM400, Thorlabs). Light pulses were generated by a pulse generator selector (16440A, Keysight).

Supporting Information

Supporting Information is available from the Wiley Online Library or from the author.

Conflict of Interest

The authors declare no conflict of interest.

Data Availability Statement

The data that support the findings of this study are available from the corresponding author upon reasonable request.

Keywords

[1] M. M. Waldrop, *Nature* **2016**, *530*, 144.

[2] S. Wang, X. Liu, P. Zhou, *Adv. Mater.* **2022**, *34*, 2106886.

[3] M. Huang, S. Li, Z. Zhang, X. Xiong, X. Li, Y. Wu, *Nat. Nanotechnol.* **2017**, *12*, 1148.

[4] K. Kobashi, R. Hayakawa, T. Chikyow, Y. Wakayama, *Nano Lett.* **2018**, *18*, 4355.

[5] R. Cheng, F. Wang, L. Yin, Z. Wang, Y. Wen, T. A. Shifa, J. He, *Nat. Electron.* **2018**, *1*, 356.

[6] D. Li, M. Chen, Z. Sun, P. Yu, Z. Liu, P. M. Ajayan, Z. Zhang, *Nat. Nanotechnol.* **2017**, *12*, 901.

[7] C. Liu, X. Yan, X. Song, S. Ding, D. W. Zhang, P. Zhou, *Nat. Nanotechnol.* **2018**, *13*, 404.

[8] J. Yi, X. Sun, C. Zhu, S. Li, Y. Liu, X. Zhu, W. You, D. Liang, Q. Shuai, Y. Wu, D. Li, A. Pan, *Adv. Mater.* **2021**, *33*, 2101036.

[9] S.-J. Lee, Z. Lin, J. Huang, C. S. Choi, P. Chen, Y. Liu, J. Guo, C. Jia, Y. Wang, L. Wang, Q. Liao, I. Shakir, X. Duan, B. Dunn, Y. Zhang, Y. Huang, X. Duan, *Nat. Electron.* **2020**, *3*, 630.

[10] W. J. Yu, Z. Li, H. Zhou, Y. Chen, Y. Wang, Y. Huang, X. Duan, *Nat. Mater.* **2013**, *12*, 246.

[11] P. Wu, D. Reis, X. S. Hu, J. Appenzeller, *Nat. Electron.* **2020**, *4*, 45.

[12] S. Ghosh, A. Varghese, K. Thakar, S. Dhara, S. Lodha, *Nat. Commun.* **2021**, *12*, 3336.

[13] M. Mongillo, P. Spathis, G. Katsaros, P. Gentile, S. De Franceschi, *Nano Lett.* **2012**, *12*, 3074.

[14] Z. Zhang, M. Passlack, G. Pitner, S. Natani, S.-K. Su, T.-A. Chao, S. L. Liew, V. D. H. Hou, C.-F. Hsu, W. E. Shipley, N. Safron, W. Doornbos, T.-E. Lee, I. Radu, A. C. Kummel, P. Bandaru, H. S. P. Wong, *Nat. Electron.* **2023**, *6*, 999.

[15] W. Fei, J. Trommer, M. C. Lemme, T. Mikolajick, A. Heinzig, *InfoMat* **2022**, *4*, 12355.

[16] S.-Y. Seo, G. Moon, O. F. N. Okello, M. Y. Park, C. Han, S. Cha, H. Choi, H. W. Yeom, S.-Y. Choi, J. Park, M.-H. Jo, *Nat. Electron.* **2020**, *4*, 38.

[17] T. Li, J. Miao, X. Fu, B. Song, B. Cai, X. Ge, X. Zhou, P. Zhou, X. Wang, D. Jariwala, W. Hu, *Nat. Nanotechnol.* **2023**, *18*, 1303.

[18] C. Pan, C.-Y. Wang, S.-J. Liang, Y. Wang, T. Cao, P. Wang, C. Wang, S. Wang, B. Cheng, A. Gao, E. Liu, K. Watanabe, T. Taniguchi, F. Miao, *Nat. Electron.* **2020**, *3*, 383.

[19] G. Wu, X. Zhang, G. Feng, J. Wang, K. Zhou, J. Zeng, D. Dong, F. Zhu, C. Yang, X. Zhao, D. Gong, M. Zhang, B. Tian, C. Duan, Q. Liu, J. Wang, J. Chu, M. Liu, *Nat. Mater.* **2023**, *22*, 1499.

[20] S. Wang, X. Chen, C. Zhao, Y. Kong, B. Lin, Y. Wu, Z. Bi, Z. Xuan, T. Li, Y. Li, W. Zhang, E. Ma, Z. Wang, W. Ma, *Nat. Electron.* **2023**, *6*, 281.

[21] X. Liang, Y. Luo, Y. Pei, M. Wang, C. Liu, *Nat. Electron.* **2022**, *5*, 859.

[22] R. Peng, Y. Wu, B. Wang, R. Shi, L. Xu, T. Pan, J. Guo, B. Zhao, C. Song, Z. Fan, C. Wang, P. Zhou, S. Fan, K. Liu, *Nat. Electron.* **2023**, *6*, 852.

[23] M.-Y. Tsai, C.-T. Huang, C.-Y. Lin, M.-P. Lee, F.-S. Yang, M. Li, Y.-M. Chang, K. Watanabe, T. Taniguchi, C.-H. Ho, W.-W. Wu, M. Yamamoto, J.-L. Wu, P.-W. Chiu, Y.-F. Lin, *Nat. Electron.* **2023**, *6*, 755.

[24] T. Kim, C. H. Choi, J. S. Hur, D. Ha, B. J. Kuh, Y. Kim, M. H. Cho, S. Kim, J. K. Jeong, *Adv. Mater.* **2023**, *35*, 2204663.

[25] K. Nomura, H. Ohta, A. Takagi, T. Kamiya, M. Hirano, H. Hosono, *Nature* **2004**, *432*, 488.

[26] R. Yang, L. Yin, J. Lu, B. Lu, X. Pi, S. Li, F. Zhuge, Y. Lu, W. Shao, Z. Ye, *ACS Appl. Mater. Interfaces* **2022**, *14*, 46866.

[27] R. Dutta, M. Naqi, Y. Cho, J. Oh, T. Kim, U. Jeong, Y. Yu, Y. Lee, S. Kim, *Adv. Funct. Mater.* **2024**, *34*, 2315058.

[28] S. Song, C. Choi, J. Ahn, J. J. Lee, J. Jang, B. S. Yu, J. P. Hong, Y. S. Ryu, Y. H. Kim, D. K. Hwang, *InfoMat* **2023**, *6*, 12479.

[29] C. Teng, Q. Yu, Y. Sun, B. Ding, W. Chen, Z. Zhang, B. Liu, H. M. Cheng, *InfoMat* **2022**, *5*, 12351.

[30] Z. Wang, P. K. Nayak, J. A. Caraveo-Frescas, H. N. Alshareef, *Adv. Mater.* **2016**, *28*, 3831.

[31] A. Liu, Y. S. Kim, M. G. Kim, Y. Reo, T. Zou, T. Choi, S. Bai, H. Zhu, Y. Y. Noh, *Nature* **2024**, *629*, 798.

[32] N. Devabharathi, S. Yadav, V. Trouillet, J. J. Schneider, *Adv. Mater. Interfaces* **2024**, *11*, 2301082.

[33] X. Zhou, Y. Shao, L. Zhang, X. Xiao, D. Han, Y. Wang, S. Zhang, *IEEE Electron Device Lett.* **2017**, *38*, 465.

[34] M. Fakhri, H. Johann, P. Görrn, T. Riedl, *ACS Appl. Mater. Interfaces* **2012**, *4*, 4453.

[35] X. Zhang, Z. Shao, X. Zhang, Y. He, J. Jie, *Adv. Mater.* **2016**, *28*, 10409.

[36] T. Kim, C. H. Choi, S. E. Kim, J.-K. Kim, J. Jang, S. Choi, J. Noh, K.-S. Park, J. Kim, S. Yoon, J. K. Jeong, *IEEE Electron Device Lett.* **2023**, *44*, 269.

[37] Y. Meng, W. Wang, R. Fan, Z. Lai, W. Wang, D. Li, X. Li, Q. Quan, P. Xie, D. Chen, H. Shao, B. Li, Z. Wu, Z. Yang, S. Yip, C. Y. Wong, Y. Lu, J. C. Ho, *Nat. Commun.* **2024**, *15*, 4440.

[38] Y. Zhang, Y. Meng, L. Wang, C. Lan, Q. Quan, W. Wang, Z. Lai, W. Wang, Y. Li, D. Yin, D. Li, P. Xie, D. Chen, Z. Yang, S. Yip, Y. Lu, C. Y. Wong, J. C. Ho, *Nat. Commun.* **2024**, *15*, 728.

[39] M. F. Al-Kuhaili, S. M. A. Durrani, E. E. Khawaja, J. Shirokoff, *J. Phys. D: Appl. Phys.* **2002**, *35*, 910.

[40] W. K. Khalef, T. R. Marzoog, A. D. Faisal, *J. Phys. Conf. Ser.* **2021**, *1795*, 012049.

[41] A. Liu, H. Zhu, W. T. Park, S. J. Kim, H. Kim, M. G. Kim, Y. Y. Noh, *Nat. Commun.* **2020**, *11*, 4309.

[42] E. Fortunato, P. Barquinha, R. Martins, *Adv. Mater.* **2012**, *24*, 2945.

[43] A. Liu, H. Zhu, Z. Guo, Y. Meng, G. Liu, E. Fortunato, R. Martins, F. Shan, *Adv. Mater.* **2017**, *29*, 1701599.

[44] G. Zhou, R. Addou, Q. Wang, S. Honari, C. R. Cormier, L. Cheng, R. Yue, C. M. Smyth, A. Laturia, J. Kim, W. G. Vandenberghe, M. J. Kim, R. M. Wallace, C. L. Hinkle, *Adv. Mater.* **2018**, *30*, 1803109.

[45] G. Qiu, A. Charnas, C. Niu, Y. Wang, W. Wu, P. D. Ye, *npj 2D Mater. Appl.* **2022**, *6*, 17.

[46] J. Tang, Q. Cao, G. Tulevski, K. A. Jenkins, L. Nela, D. B. Farmer, S.-J. Han, *Nat. Electron.* **2018**, *1*, 191.

[47] D. Fan, W. Li, H. Qiu, Y. Xu, S. Gao, L. Liu, T. Li, F. Huang, Y. Mao, W. Zhou, W. Meng, M. Liu, X. Tu, P. Wang, Z. Yu, Y. Shi, X. Wang, *Nat. Electron.* **2023**, *6*, 879.

[48] N. Hempel de Ibarra, M. Vorobyev, R. Menzel, *J. Comp. Physiol., A* **2014**, *200*, 411.

[49] Z. Zhang, S. Wang, C. Liu, R. Xie, W. Hu, P. Zhou, *Nat. Nanotechnol.* **2022**, *17*, 27.

[50] G. Kresse, J. Furthmüller, *Comp. Mater. Sci.* **1996**, *6*, 15.

[51] J. P. Perdew, K. Burke, M. Ernzerhof, *Phys. Rev. Lett.* **1996**, *77*, 3865.